Optics Letters

Fast hyperspectral phase and amplitude imaging in scattering tissue

Cong Ba,* Jean-Marc Tsang, and Jerome Mertz

Biomedical Engineering Department, Boston University, 44 Cummington Mall, Boston, Massachusetts 02215, USA
**Corresponding author: bacong@bu.edu*

Received 27 February 2018; accepted 22 March 2018; posted 26 March 2018 (Doc. ID 324908); published 24 April 2018

Hyperspectral imaging in scattering tissue generally suffers from low light collection efficiency. In this Letter, we propose a microscope based on Fourier transform spectroscopy and oblique back-illumination microscopy that provides hyperspectral phase and amplitude images of thick, scattering samples with high throughput. Images can be acquired at >0.1 Hz rates with spectral resolution better than 200 cm^{-1}, over a wide spectral range of 450–1700 nm. Proof-of-principle demonstrations are presented with chorioallantoic membrane of a chick embryo, illustrating the possibility of high-resolution hemodynamics imaging in thick tissue, based on transmission contrast.

OCIS codes: (110.4234) Multispectral and hyperspectral imaging; (300.6300) Spectroscopy, Fourier transforms; (120.6200) Spectrometers and spectroscopic instrumentation.

https://doi.org/10.1364/OL.43.002058

Hyperspectral imaging (HSI) combines traditional imaging with spectroscopy to provide simultaneous spatio-spectral information in the form of a 3D (x, y, λ) image cube [1,2]. HSI has been widely used in astronomy [3], food analysis [4], and other domains [5,6], and is quickly gaining interest in biomedical optics. However, the highly scattering nature of biological tissue poses a challenge for conventional spectral acquisition methods. For example, diffuse light from tissue cannot be efficiently focused into slit-based spectrometers [7,8], causing signal collection efficiency to be low. Similarly, tunable bandpass filters (BFs) require quasi-collimated light [9,10], also making them ill suited for the collection of diffuse signal.

A better strategy, when dealing with scattering tissue, is to perform spectral discrimination on the illumination side of the sample rather than the detection side. A particularly fast solution involves frequency multiplexing (e.g., [11]), wherein different wavelengths in a broadband illumination beam are tagged with different modulation frequencies. A single, large-area photodiode can then be used to efficiently collect the scattered signal, and the spectral information can be retrieved by temporal Fourier transformation. We implemented this Fourier-transform spectroscopy (FTS) approach with a supercontinuum laser modulated by a Michelson interferometer. Although HSI has previously been demonstrated with FTS [12,13], the interferometer in these demonstrations was on the detection side of the sample, often requiring specialized interferometers to increase collection efficiency [14,15]. In our design, the spectrometer is on the illumination side of the sample, greatly facilitating alignment and enhancing throughput. Moreover, multiplexing provides the so-called "Fellgett advantage" [16], which is beneficial in the long wavelength range where detectors are noisy.

In this work, we combined illumination-side FTS with scanning oblique back-illumination microscopy (OBM) [17]. OBM is a technique that provides simultaneous, optically sectioned phase and amplitude contrast in arbitrarily thick scattering samples, and can be implemented as an add-on with any scanning microscope [18,19]. We note that, although HSI has been successfully used to extract spectral information arising from absorption [20,21], reflection [12], fluorescence emission [7,22], and Raman scattering [23,24] in various modalities, it has, to our knowledge, not been demonstrated with phase imaging techniques.

Our setup is shown in Fig. 1. A supercontinuum laser (Fianium WL-SC-400-4) provides broadband illumination (400 nm to 2400 nm; power at the sample less than 200 mW), which is directed to a scanning Michelson interferometer where a moving mirror is mounted on a piezoelectric translation stage (nPoint nPX300). The modulated illumination is then sent to a homebuilt scanning microscope comprising a resonant x–y galvanometer (Cambridge Technology, CRS 12 kHz and 6215H). Following the principle of OBM, the back-scattered illumination is detected off axis through two 1.5 mm-core fibers (Thorlabs FP1500ERT) onto which mini-prisms (Edmund Optics #32-526) are optically cemented. The left/right signals are detected with photodiodes (PD1 and PD2) and digitized (National Instruments 5734), leading to a frame rate at 256 × 256 pixels of 92 fps in bidirectional mode. Si detectors (Thorlabs PDA36A) or InGaS detectors (Thorlabs, PDA20CS) are used, depending on the wavelength range.

To correct for the intensity fluctuations arising from the laser itself, a third photodiode (PD3) records the laser power for reference. Also, to validate our FTS technique, we introduced an auxiliary illumination path through a bank of 17 BFs (Edmund Optics, Hard Coated OD 4 Series, center

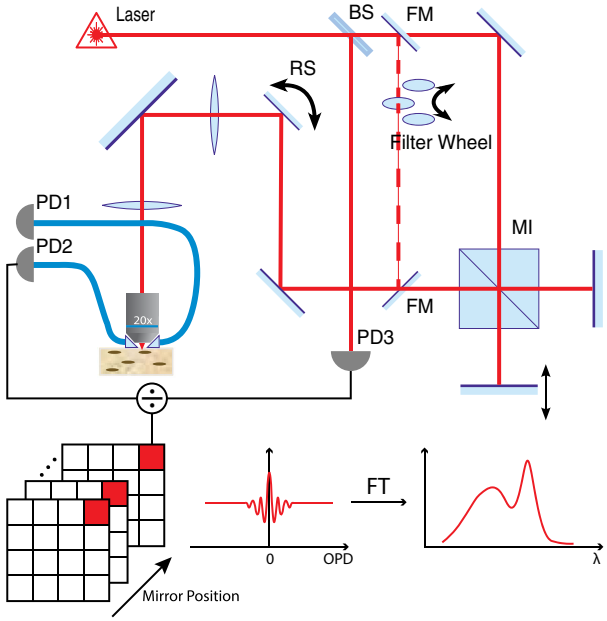

Fig. 1. Schematic of our FT-OBM system. FM, flip mirror; MI, Michelson interferometer; BS, 90/10 beam splitter; RS, resonant scanner; PD, photodiode. Additional long-/short-pass and neutral density filters are not shown explicitly. The division is computed numerically. Signals from PD1 and PD2 undergo identical processing procedures.

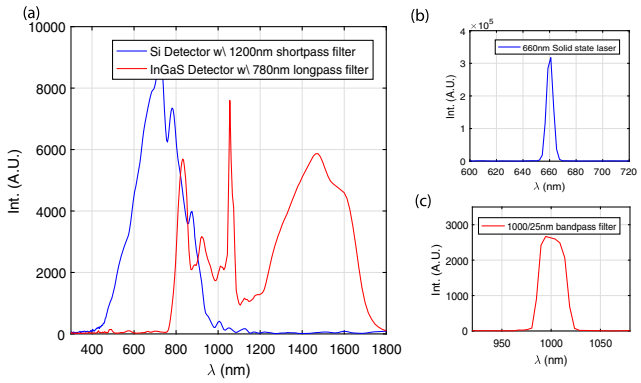

Fig. 2. Laser spectra measured with a Teflon block sample. (a) Neutral spectral envelope of the supercontinuum source measured with Si detector and InGaS detector separately. (b) 660 nm solid-state laser measured with Si detector, showing a FWHM of <7 nm. (c) Spectrum of bandpass-filtered (1000/25) supercontinuum laser, measured with InGaS detector, showing a FWHM of 35 nm.

wavelengths 600 nm to 1000 nm with step size and bandwidth both 25 nm), mounted on three motorized filter wheels (Thorlabs, FW102C/FW212C) programmed with an Arduino micro-controller. Switching between interferometer and programmable-filter paths is effected with a pair of flip mirrors.

When the BF pathway is selected, a set of 2 × 17 hyperspectral images is acquired within 20 s, with spectral resolution 25 nm limited by the BFs. When the FTS pathway is selected, we linearly scan the moving mirror at 10 μm/s and continuously acquire images for 10 s, obtaining 920 frames with a total mirror travel of 100 μm. From sampling theory, the minimum detectable wavelength is twice the optical pathlength difference (OPD) step size, $\lambda_{\min} = 2\Delta\mathrm{OPD}$, which in our case is 434 nm. The spectral resolution is then given by $\Delta\nu = 1/\mathrm{OPD}_{\max}$ and $\Delta\lambda = \lambda \cdot \Delta\nu/\nu$. In our experiment, since we perform two-sided scans with the Michelson interferometer, the maximum OPD is 100 μm, yielding a spectral resolution of about 10 nm at 700 nm. Note that better resolution could be achieved by sacrificing the number of pixels or acquisition speed. The interferograms obtained for all pixels are apodized with a Blackman–Harris window, phase corrected, zero padded, and Fourier transformed by fast Fourier transform (FFT) [25]. The spectra are obtained by taking absolute values. Hyperspectral images are then constructed by binning the spectra into user-defined wavelength ranges. For comparison, the spectral binning can be set to 25 nm, thus leading to reconstructed images that are theoretically equivalent to those obtained with the BF pathway, differing only in acquisition time and SNR.

To verify the performance of our system, we imaged a solid Polytetrafluoroethylene (PTFE) (Teflon) block, which is usually considered wavelength neutral. For this measurement, we acquired 128 × 128 images to double our sampling rate (fps), corresponding to a 217 nm minimum detectable wavelength. Each spectrum shown in Fig. 2 is averaged over 128 consecutive pixels (one row). When an Si detector is used, the reconstructed spectrum spans 440 nm to 1000 nm, limited by the laser output and detector wavelength range. When an InGaS detector is used, this range is extended to beyond 1700 nm. Note that when imaging aqueous biological samples, an additional 1300 nm shortpass filter is introduced in the illumination path to avoid excessive absorption. Figure 2 shows spectra of a solid-state 660 nm laser (Si detector) and of the supercontinuum laser sent through a 1000/25 BF (InGaS detector), confirming theory-limited spectral resolution.

Finally, for each pair of raw images in a given wavelength range (in either FT- or BF-OBM), we construct phase and amplitude images. To do this, raw images are first normalized by Gaussian low-pass-filtered versions of themselves to correct for the globally non-uniform illumination, thus "flattening" the images. The normalized images are then summed to produce an amplitude-only image, or subtracted and divided by the sum to produce a phase-only image (more precisely, a phase-gradient-only image—see [17] for details). The two contrasts can be readily overlaid, since they are inherently co-registered.

To demonstrate the possibility of *in vivo* tissue imaging, a chick embryo chorioallantoic membrane (CAM) was imaged with Si detectors (450–1000 nm). Fertilized eggs (Carolina Biological Supply) were stored in an incubator at 37°C and 50% humidity. A piece of the shell and shell membrane was removed at post-fertilization day 9, exposing the embryo and CAM. Imaging of CAM was performed with a water immersion objective [Olympus UMPlanFL W 10×, numerical aperture (NA) = 0.3]. Figure 3 shows an example of raw and processed OBM images. The raw images are obtained by FTS, reconstructed with a 500–600 nm passband. Individual cells and blood vessels both can be clearly seen in the phase image. The blood vessels appear dark in the amplitude image, as the result of hemoglobin absorption. To highlight this feature, we reconstructed the absorption coefficient of hemoglobin based on the measured diameter of the blood vessel [see Fig. 3(d)], where two regions inside and outside of the blood vessel, each 3 × 3 pixels in size, were used to calculate the transmission ratio. Our reconstructed absorption spectrum

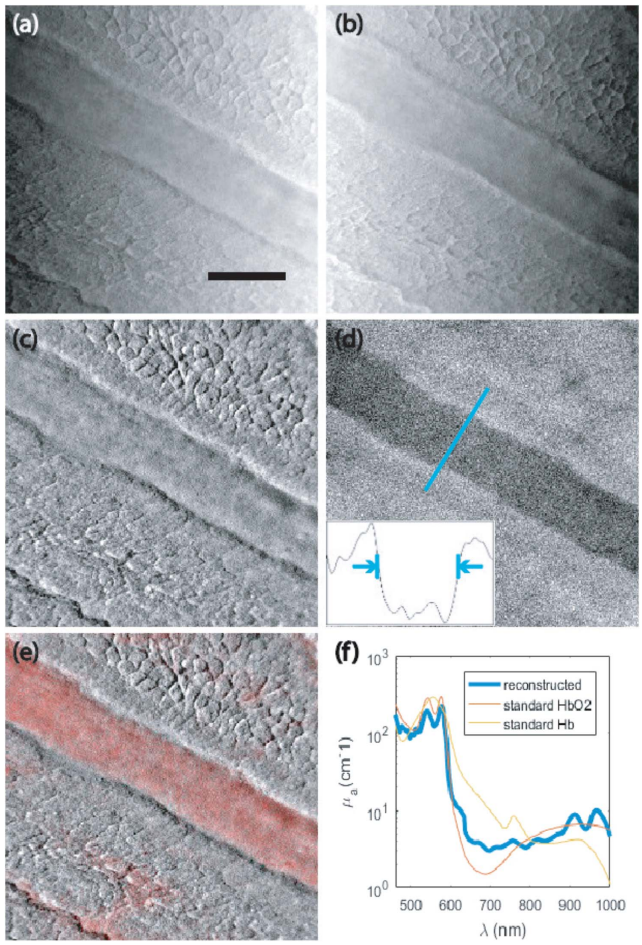

Fig. 3. Example showing the raw and processed OBM images of a CAM sample. Scale bar: 100 μm. (a), (b) A pair of raw OBM images acquired by FT-OBM and reconstructed at 500–600 nm. (c)–(e) Processed phase-only, amplitude-only, and combined contrast images, respectively. (f) Reconstructed hemoglobin absorption coefficient.

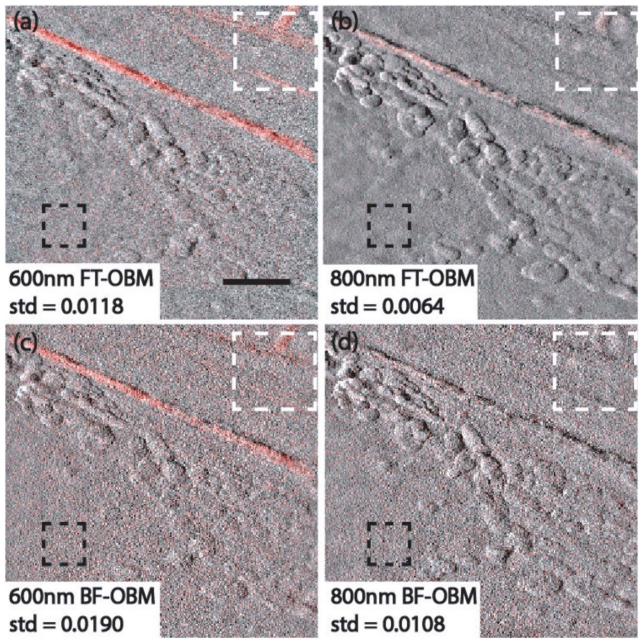

Fig. 4. Comparison of dual-contrast images acquired with FT-OBM and BF-OBM at 600 nm and 800 nm. FT-OBM images exhibit lower noise levels, as illustrated by the std in the featureless zones indicated by black squares. Scale bar: 100 μm.

roughly lies between the oxygenated and de-oxygenated spectra reported in the literature [26].

It should be emphasized that the optical imaging of blood oximetry in arbitrarily thick tissue and with high spatial resolution is not always straightforward. Alternative techniques, such as optical coherence tomography (OCT), are based on reflection contrast and thus rely on strong, specular-like reflection from the back walls of blood vessels to enable the illumination to perform a double pass through the vessels. Moreover, coarse spectral binning is required to avoid undermining axial resolution [27]. In contrast, OBM is inherently based on transmission contrast [17]. The illumination performs a single pass though the blood vessels, and spatio-spectral resolution is not compromised. Moreover, OBM is speckle free.

In addition to the practical advantage that spectral scanning with an interferometer is faster than with a battery of BFs, FT-OBM offers a more fundamental speed advantage. Specifically, it is well known that, for conditions of equal power, acquisition time, and spectral resolution, multiplexing provides no SNR advantage when the detection is shot-noise limited. But in our case, FT-OBM does not systematically reject light with BFs, and thus utilizes power more efficiently than BF-OBM, enabling reduced acquisition times for equal SNR. To demonstrate this, we made comparisons of FT-OBM and BF-OBM images over equal fields-of-view (FOVs), where a 25 nm numerical passband was applied to our FT-OBM reconstructions. Dual-contrast images in two wavelength bands are overlaid in Fig. 4. The images from both techniques are similar, as expected, but the noise level of FT-OBM is manifestly lower than that of BF-OBM, even though the total acquisition time for the former was half that for the latter, over the same frequency range. For example (white squares), at 600 nm, some blood vessels are apparent in amplitude but not so much in phase due to increased noise. At 800 nm where blood absorption is reduced, the amplitude contrast disappears while the phase contrast improves. Note that since the signals in phase-gradient images vary about zero; we report here only their standard deviations (std).

To demonstrate the capacity of our system to image over an extended spectral range, we imaged a mouse colon sample. A freshly excised colon was slit along its length and opened to expose the intestinal glands in the epithelial lumen. The tissue was placed on a Teflon block to ensure that the scattering medium was thick enough to re-direct laser illumination back toward the surface. Colon sample imaging was performed with an air-immersion objective (Olympus LUCPlanFL 20×, NA = 0.45). The same FOV was imaged with both Si and InGaS detectors, enabling us to evaluate the effect of longer wavelengths on phase contrast—see Fig. 5. Manifestly, the noise was not significantly worsened at longer wavelengths despite the use of noisier detectors (in accord with the Fellgett advantage). More interestingly, the contrast also appeared similar, and the maximum penetration depths were found to be roughly the same, about 100 μm, beyond which phase contrast was lost. A possible explanation is that the reduced scattering at

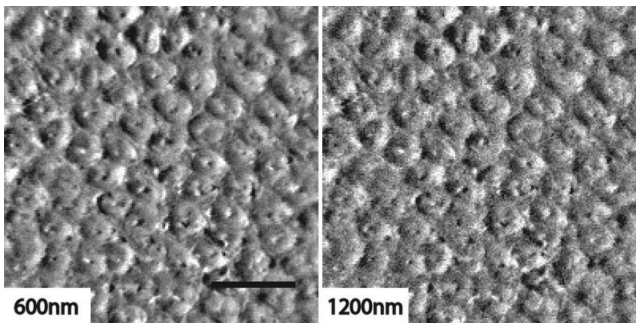

Fig. 5. Comparison of phase-contrast-only images of a mouse colon sample at 600 nm and 1200 nm. Scale bar: 100 μm.

longer wavelengths, while enabling more ballistic light to arrive at the focal plane, produces less scattered signal from this focal plane. The two effects seem to roughly counterbalance as wavelength is increased.

As an aside, we note that when performing FT-OBM at longer wavelengths, intentional undersampling can be used to double the acquisition rate. This technique is widely used for sampling bandpassed signals [28]. Specifically, the modulation frequency associated with 1300 nm is more than half that associated with 780 nm. Thus, sampling at half of Nyquist rate required for 780 nm, which causes aliasing, nevertheless does not cause overlap in the useful spectral range. This enables us to double the scan speed of the moving mirror, which in turn enables us to halve the acquisition time without sacrificing spectral resolution. Alternatively, we can hold the acquisition time fixed and double the spectral resolution.

In summary, we have demonstrated a high-resolution FTS-based HSI technique that is able to retrieve spectral information from scattering tissue in a simple and robust manner, providing both phase and amplitude contrast. However, our technique is not without problems. The most important problem we faced comes from noise. Noise in our system mainly arises from three sources: laser power fluctuations, laser spectrum noise, and cross-channel shot noise from multiplexing. Regarding the first source, a supercontinuum laser is intrinsically very noisy. Moreover, our laser pulse rate (40 MHz) is only five times our imaging pixel rate (~8 MHz), meaning that in the absence of synchronization (the case here), the number of pulses per pixel can vary. To alleviate this problem, we introduced a third photodiode to directly monitor the laser power and serve as a normalizing reference. Unfortunately, this cannot correct for pulse-to-pulse intra-spectrum variations endemic to the supercontinuum generation process in microstructured fibers [29]. Our only recourse to alleviate this laser spectrum noise is to use broader passbands when binning our spectra, thus performing wavelength averaging at the cost of degraded spectral resolution. Finally, another fundamental noise comes from multiplexing itself. When multiplexing, shot noise is uniformly distributed across all the spectral bands. As such, spectral regions where the signal is weak are subject to increased shot noise from regions where the signal is strong. Application of spectrum-shaping filters in the illumination arm of the instrument may contribute to resolve this issue; however, this is beyond the scope of our present work.

Yet another issue to consider when dealing with such a broad wavelength range is the issue of chromatic dispersion of the microscope components themselves. Depending on the application, this can be advantageous, giving rise to an effective extended depth of field, or it can be disadvantageous, when spectral co-registration is required. It should be noted that in our case, this issue did not appear to be significant. Indeed, despite all its drawbacks, FT-OBM seemed to quite clearly outperform BF-OBM in all respects. In particular, for equal acquisition time, spectral range and resolution can be easily adjusted simply by adjusting FTS scan range and sampling rate, which is not the case when using a fixed set of BFs. But the key advantage of FT-OBM comes from its use of large, non-imaging detectors, allowing it to readily access broad wavelength ranges with high collection efficiency, and making it particularly adapted to HSI in thick, scattering tissue.

Funding. National Institutes of Health (NIH) (R01CA182939).

REFERENCES

1. N. A. Hagen and M. W. Kudenov, Opt. Eng. **52**, 090901 (2013).
2. L. Gao and R. T. Smith, J. Biophoton. **8**, 441 (2015).
3. P. Jacquinot, J. Opt. Soc. Am. **44**, 761 (1954).
4. G. ElMasry, D.-W. Sun, and P. Allen, J. Food Eng. **110**, 127 (2012).
5. J. Lelieveld, J. Evans, M. Fnais, D. Giannadaki, and A. Pozzer, Nature **525**, 367 (2015).
6. J. R. Norris, R. J. Allen, A. T. Evan, M. D. Zelinka, C. W. O'Dell, and S. A. Klein, Nature **536**, 72 (2016).
7. M. B. Sinclair, D. M. Haaland, J. A. Timlin, and H. D. Jones, Appl. Opt. **45**, 6283 (2006).
8. J. M. Lerner, Cytometry Part A **69**, 712 (2006).
9. N. Gat, Proc. SPIE **4056**, 50 (2000).
10. S. C. Gebhart, R. C. Thompson, and A. Mahadevan-Jansen, Appl. Opt. **46**, 1896 (2007).
11. C.-S. Liao, P. Wang, P. Wang, J. Li, H. J. Lee, G. Eakins, and J.-X. Cheng, Sci. Adv. **1**, e1500738 (2015).
12. J. Li and R. K. Chan, Opt. Lett. **35**, 3330 (2010).
13. S. Jin, W. Hui, Y. Wang, K. Huang, Q. Shi, C. Ying, D. Liu, Q. Ye, W. Zhou, and J. Tian, Sci. Rep. **7**, 45209 (2017).
14. H. Choi, D. Wadduwage, P. T. Matsudaira, and P. T. So, Biomed. Opt. Express **5**, 3494 (2014).
15. A. R. Harvey and D. W. Fletcher-Holmes, Opt. Express **12**, 5368 (2004).
16. P. Fellgett, J. Opt. Soc. Am. **39**, 970 (1949).
17. T. N. Ford, K. K. Chu, and J. Mertz, Nat. Methods **9**, 1195 (2012).
18. J. Mertz, A. Gasecka, A. Daradich, I. Davison, and D. Coté, Biomed. Opt. Express **5**, 407 (2014).
19. C. Ba, M. Palmiere, J. Ritt, and J. Mertz, Biomed. Opt. Express **7**, 3403 (2016).
20. E. N. Lewis, P. J. Treado, R. C. Reeder, G. M. Story, A. E. Dowrey, C. Marcott, and I. W. Levin, Anal. Chem. **67**, 3377 (1995).
21. J. Y. Lee, M. L. Clarke, F. Tokumasu, J. F. Lesoine, D. W. Allen, R. Chang, M. Litorja, and J. Hwang, IEEE J. Sel. Top. Quantum Electron. **18**, 1130 (2012).
22. A. J. Radosevich, M. B. Bouchard, S. A. Burgess, B. R. Chen, and E. M. Hillman, Opt. Lett. **33**, 2164 (2008).
23. D. Zhang, P. Wang, M. N. Slipchenko, D. Ben-Amotz, A. M. Weiner, and J.-X. Cheng, Anal. Chem. **85**, 98 (2012).
24. E. T. Garbacik, J. L. Herek, C. Otto, and H. L. Offerhaus, J. Raman Spectrosc. **43**, 651 (2012).
25. P. R. Griffiths and J. A. De Haseth, *Fourier Transform Infrared Spectrometry* (Wiley, 2007), Vol. **171**.
26. S. Prahl, *Optical Absorption of Hemoglobin* (1999).
27. J. Yi, Q. Wei, W. Liu, V. Backman, and H. F. Zhang, Opt. Lett. **38**, 1796 (2013).
28. R. G. Vaughan, N. L. Scott, and D. R. White, IEEE Trans. Signal Process. **39**, 1973 (1991).
29. K. L. Corwin, N. R. Newbury, J. M. Dudley, S. Coen, S. A. Diddams, K. Weber, and R. Windeler, Phys. Rev. Lett. **90**, 113904 (2003).